A.K. POPOV[1]
V.M. SHALAEV[2,✉]

Negative-index metamaterials: second-harmonic generation, Manley–Rowe relations and parametric amplification

[1] Department of Physics and Astronomy and Department of Chemistry, University of Wisconsin-Stevens Point, Stevens Point, WI 54481-3897, USA
[2] School of Electrical and Computer Engineering, Purdue University, West Lafayette, IN 47907-2035, USA

ABSTRACT Second harmonic generation and optical parametric amplification in negative-index metamaterials (NIMs) are studied. The opposite directions of the wave vector and the Poynting vector in NIMs results in a "backward" phase-matching condition, causing significant changes in the Manley–Rowe relations and spatial distributions of the coupled field intensities. It is shown that absorption in NIMs can be compensated by backward optical parametric amplification. The possibility of distributed-feedback parametric oscillation with no cavity has been demonstrated. The feasibility of the generation of entangled pairs of left- and right-handed counter-propagating photons is discussed.

PACS 78.67.-n; 42.65.Ky; 42.65.Lm

1 Introduction

Recent demonstration of a negative refractive index for metamaterials in the optical range [1, 2] opens new avenues for optics and especially nonlinear optics. In parallel with progress for metal-dielectric metamaterials, experimental demonstrations of negative refraction in the near IR range have been made in a GaAs-based photonic crystal [3], and in Si-polyimide photonic crystals [4]. Negative refractive-index metamaterials (NIMs) are also referred to as left-handed materials (LHMs). The sufficient (but not necessary) condition for a negative refractive index is simultaneous negative dielectric permittivity $\varepsilon(\omega)$ and negative magnetic permeability $\mu(\omega)$ [5, 6]. Negative magnetic permeability in the optical range has been demonstrated in [7–9]. NIMs exhibit highly unusual optical properties and promise a great variety of unprecedented applications. Optical magnetization, which is normally ignored in linear and nonlinear-optics of the ordinary, positive-index materials (PIMs) (i.e., right-handed materials, RHMs) plays a crucial role in NIMs.

The main emphasis in the studies of NIMs has been placed so far on linear optical effects. Recently it has been shown that NIMs including structural elements with non-symmetric current–voltage characteristics can possess a nonlinear magnetic response at optical frequencies [10–13], and

✉ Fax: +765-494-6951, E-mail: shalaev@purdue.edu

thus combine unprecedented linear and nonlinear electromagnetic properties. Important properties of second harmonic generation (SHG) in NIMs in the constant-pump approximation were discussed in [14] for semi-infinite materials and in [15] for a slab of a finite thickness. The propagation of microwave radiation in nonlinear transmission lines, which are the one-dimensional analog of NIMs, was investigated in [16]. The possibility of exact phase-matching for waves with counter-propagating energy-flows has been shown in [17] for the case when the fundamental wave falls in the negative-index frequency domain and the SH wave lies in the positive-index domain. The possibility of the existence of multistable nonlinear effects in SHG was also predicted in [17].

As will be seen from our considerations below, the phase-matching of normal and backward waves is inherent for nonlinear optics of NIMs. We note here that the important advantages of interaction schemes involving counter-directed Poynting vectors in the process of optical parametric amplification in ordinary RHMs were discussed in early papers [18–20]. However, in RHMs such schemes impose severe limitations on the frequencies of the coupled waves because of the requirement that one of the waves has to be in the far-infrared range.

Absorption is one of the biggest problems to be addressed for the practical applications of NIMs. In [14, 15], a transfer of the near-field image into the SH frequency domain, where absorption is typically much less, was proposed as a means to overcome dissipative losses and thus enable the superlens.

In this paper, we demonstrate unusual characteristics in the spatial distribution of the energy exchange between the fundamental and second-harmonic waves. Both semi-infinite and finite-length NIMs are considered and compared with each other and with ordinary PIMs. Our analysis is based on the solution to equations for the coupled waves propagating in lossless NIMs beyond the constant-pump approximation. The Manley–Rowe relations for NIMs are analyzed and they are shown to be strikingly different from those in PIMs. We also propose a new means of compensating losses in NIMs by employing optical parametric amplification (OPA). This can be realized by using control electromagnetic waves (with frequencies outside the negative-index domain), which provide the loss-balancing OPA inside the negative-index frequency domain. We also predict laser oscillations without a cavity for

frequencies in the negative-index domain and the possibility of the generation of entangled pairs of counter-propagating right- and left-handed photons.

The paper is organized as follows. Section 2 discusses the unusual spatial distribution of the field intensities for SHG in finite and semi-infinite slabs of NIMs. The Manley–Rowe relations are derived and discussed here. The feasibility of compensating losses in NIMs by using the OPA is considered in Sect. 3. In this section we also study cavity-less oscillations based on distributed feedback. Finally, a summary of the obtained results concludes the paper.

2   Second harmonic generation in NIMs

2.1   *Wave vectors and Poynting vectors in NIMs*

We consider a loss-free material, which is left-handed at the fundamental frequency ω_1 ($\varepsilon_1 < 0$, $\mu_1 < 0$), whereas it is right-handed at the SH frequency $\omega_2 = 2\omega_1$ ($\varepsilon_2 > 0$, $\mu_2 > 0$). The relations between the vectors of the electrical, E, and magnetic, H, field components and the wave-vector k for a traveling electromagnetic wave,

$$E(r, t) = E_0(r) \exp[i(k \cdot r - \omega t)] + c.c. , \tag{1}$$

$$H(r, t) = H_0(r) \exp[i(k \cdot r - \omega t)] + c.c. , \tag{2}$$

are given by the following formulas

$$k \times E = (\omega/c)\mu H, \quad k \times H = -(\omega/c)\varepsilon E, \tag{3}$$

$$\sqrt{\varepsilon} E(r, t) = -\sqrt{\mu} H(r, t), \tag{4}$$

which follow from Maxwell's equations. These expressions show that the vector triplet E, H and k forms a right-handed system for the SH wave and a left-handed system for the fundamental beam. Simultaneously negative $\varepsilon_i < 0$ and $\mu_i < 0$ result in a negative refractive index $n = -\sqrt{\mu\varepsilon}$. As seen from (1) and (2), the phase velocity v_{ph} is co-directed with k and is given by $v_{ph} = (k/k)(\omega/k) = (k/k)(c/|n|)$, where $k^2 = n^2(\omega/c)^2$. In contrast, the direction of the energy flow (Poynting vector) S with respect to k depends on the signs of ε and μ:

$$S(r, t) = \frac{c}{4\pi}[E \times H]\frac{c^2}{4\pi\omega\varepsilon}[H \times k \times H] =$$
$$= \frac{c^2 k}{4\pi\omega\varepsilon}H^2 = \frac{c^2 k}{4\pi\omega\mu}E^2. \tag{5}$$

As mentioned, we assume here that all indices of ε, μ and n are real numbers. Thus, the energy flow S_1 at ω_1 is directed opposite to k_1, whereas S_2 is co-directed with k_2.

2.2   *SHG: Basic equations and the Manley–Rowe relations*

We assume that an incident flow of fundamental radiation S_1 at ω_1 propagates along the z-axis, which is normal to the surface of a metamaterial. According to (5), the phase of the wave at ω_1 travels in the reverse direction inside the NIM (the upper part of Fig. 1). Because of the phase-matching requirement, the generated SH radiation also travels backward with energy flow in the same backward direction. This is in
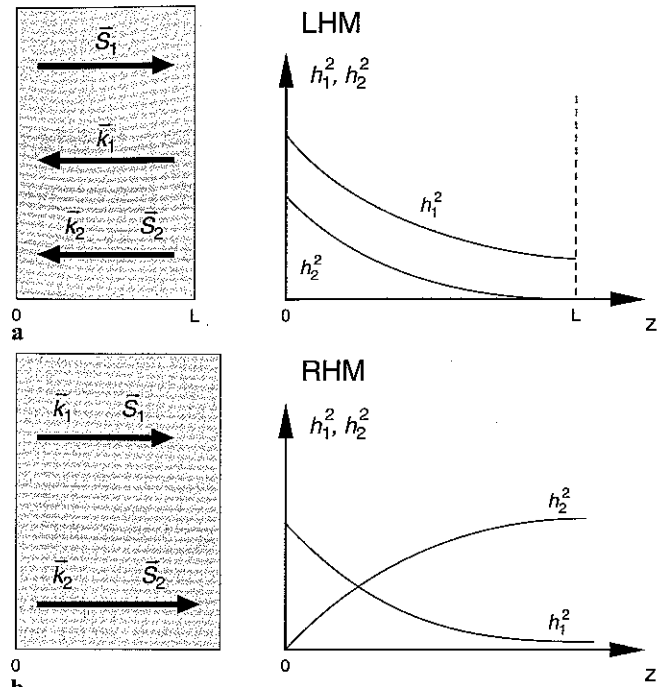

FIGURE 1   SHG geometry and the difference between SHG in LHM and RHM slabs

contrast with the standard coupling geometry in a PIM (the lower part of Fig. 1). Following the method of [17], we assume that a nonlinear response is primarily associated with the magnetic component of the waves. Then the equations for the coupled fields inside a NIM in the approximation of slow-varying amplitudes acquire the form:

$$\frac{dA_2}{dz} = i\frac{\varepsilon_2\omega_2^2}{k_2 c^2}4\pi\chi_{eff}^{(2)}A_1^2\exp(-i\Delta kz), \tag{6}$$

$$\frac{dA_1}{dz} = i\frac{\varepsilon_1\omega_1^2}{k_1 c^2}8\pi\chi_{eff}^{(2)}A_2 A_1^*\exp(i\Delta kz). \tag{7}$$

Here, $\chi_{eff}^{(2)}$ is the effective nonlinear susceptibility, $\Delta k = k_2 - 2k_1$ is the phase mismatch, and A_2 and A_1 are the slowly varying amplitudes of the waves with the phases traveling against the z-axis:

$$H_j(z, t) = A_j\exp\left[-i(k_j z + \omega_j t)\right] + c.c., \tag{8}$$

where, $\omega_2 = 2\omega_1$ and $k_{1,2} > 0$ are the moduli of the wave-vectors directed against the z-axis. We note that according to (4) the corresponding equations for the electric components can be written in a similar form, with ε_j substituted by μ_j and vice versa. The factors μ_j were usually assumed to be equal to one in similar equations for PIMs. However, this assumption does not hold for the case of NIMs, and this fact dramatically changes many conventional electromagnetic relations. The Manley–Rowe relations [21] for the field intensities and for the energy flows follow from (5)–(7):

$$\frac{k_1}{\varepsilon_1}\frac{d|A_1|^2}{dz} + \frac{k_2}{2\varepsilon_2}\frac{d|A_2|^2}{dz} = 0, \quad \frac{d|S_1|}{dz} - \frac{d|S_2|}{dz} = 0. \tag{9}$$

The latter equation accounts for the difference in the signs of ε_1 and ε_2, which brings radical changes to the spatial dependence of the field intensities discussed below.

We focus on the basic features of the process and ignore the dissipation of both waves inside the nonlinear medium; in addition, we assume that the phase matching condition $k_2 = 2k_1$ is fulfilled. The spatially-invariant form of the Manley–Rowe relations follows from (30):

$$|A_1|^2/\varepsilon_1 + |A_2|^2/\varepsilon_2 = C, \tag{10}$$

where C is an integration constant. With $\varepsilon_1 = -\varepsilon_2$, which is required for the phase matching, (10) predicts that the difference between the squared amplitudes remains constant through the sample

$$|A_1|^2 - |A_2|^2 = C, \tag{11}$$

as schematically depicted in the upper part of Fig. 1. This is in complete opposition to the requirement that the sum of the squared amplitudes is constant in the analogous case in a PIM, as schematically shown in the lower part of Fig. 1. We now introduce the real phases and amplitudes as $A_{1,2} = h_{1,2} \exp(i\varphi_{1,2})$. Then the equations for the phases, which follow from (6) and (7), show that if any of the fields become zero at any point, the integral (10) corresponds to the solution with the constant phase difference $2\varphi_1 - \varphi_2 = \pi/2$ over the entire sample.

The equations for the slowly-varying amplitudes corresponding to the ordinary coupling scheme in a PIM, shown in the lower part of Fig. 1, are readily obtained from (6)–(8) by changing the signs of k_1 and k_2. This does not change the integral (10); more importantly, the relation between ε_1 and ε_2 required by the phase matching now changes to $\varepsilon_1 = \varepsilon_2$, where both constants are positive. The phase difference remains the same. Because of the boundary conditions $h_1(0) = h_{10}$ and $h_2(0) = h_{20} = 0$, the integration constant becomes $C = h_{10}^2$. Thus, the equations for the real amplitudes in the case of a PIM acquire the form:

$$h_1(z) = \sqrt{h_{10}^2 - h_2(z)^2}, \tag{12}$$

$$dh_2/dz = \kappa \left[h_{10}^2 - h_2(z)^2 \right], \tag{13}$$

with the known solution

$$h_2(z) = h_{10} \tanh(z/z_0), \tag{14}$$

$$h_1(z) = h_{10}/\cosh(z/z_0), \; z_0 = [\kappa h_{10}]^{-1}. \tag{15}$$

Here, $\kappa = (\varepsilon_2 \omega_2^2/k_2 c^2) 4\pi \chi_{\text{eff}}^{(2)}$. The solution has the same form for an arbitrary slab thickness, as shown schematically in the lower part of Fig. 1.

2.3 SHG in a NIM slab

Now consider phase-matched SHG in a lossless NIM slab of a finite length L. Equations (6) and (11) take the form:

$$h_1(z)^2 = C + h_2(z)^2, \tag{16}$$

$$dh_2/dz = -\kappa \left[C + h_2(z)^2 \right]. \tag{17}$$

Taking into account the different boundary conditions in a NIM as compared to a PIM, $h_1(0) = h_{10}$ and $h_2(L) = 0$, the solution to these equations is as follows

$$h_2 = \sqrt{C} \tan \left[\sqrt{C}\kappa(L - z) \right], \tag{18}$$

$$h_1 = \sqrt{C}/\cos \left[\sqrt{C}\kappa(L - z) \right], \tag{19}$$

where the integration parameter C depends on the slab thickness L and on the amplitude of the incident fundamental radiation as

$$\sqrt{C}\kappa L = \arccos \left(\sqrt{C}/h_{10} \right). \tag{20}$$

Thus, the spatially invariant field intensity difference between the fundamental and SH waves in NIMs depends on the slab thickness, which is in strict contrast with the case in PIMs. As seen from (16), the integration parameter $C = h_1(z)^2 - h_2(z)^2$ now represents the deviation of the conversion efficiency $\eta = h_{20}^2/h_{10}^2$ from unity: $(C/h_{10}^2) = 1 - \eta$. Figure 2 shows the dependence of this parameter on the conversion length $z_0 = (\kappa h_{10})^{-1}$. The figure shows that for the conversion length of $z_0 = (2.5)$, the NIM slab, which acts as nonlinear mirror, provides about 80% conversion of the fundamental beam into a reflected SH wave. Figure 3 depicts the field distribution along the slab. One can see from the figure that with an increase in slab length (or intensity of the fundamental wave), the gap between the two plots decreases while the conversion efficiency increases (comparing the main plot and the inset).

2.4 SHG in a semi-infinite NIM

Now we consider the case of a semi-infinite NIM at $z > 0$. Since both waves disappear at $z \to \infty$ due to the entire conversion of the fundamental beam into SH, $C = 0$. Then (16) and (17) for the amplitudes take the simple form

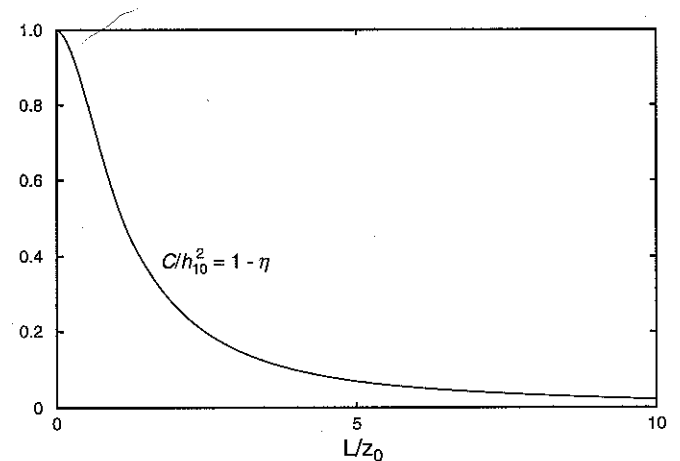$$h_2(z) = h_1(z), \tag{21}$$

$$dh_2/dz = -\kappa h_2^2. \tag{22}$$

FIGURE 2 The normalized integration constant C/h_{10}^2 and the energy conversion efficiency η vs. the normalized thickness of a NIM slab
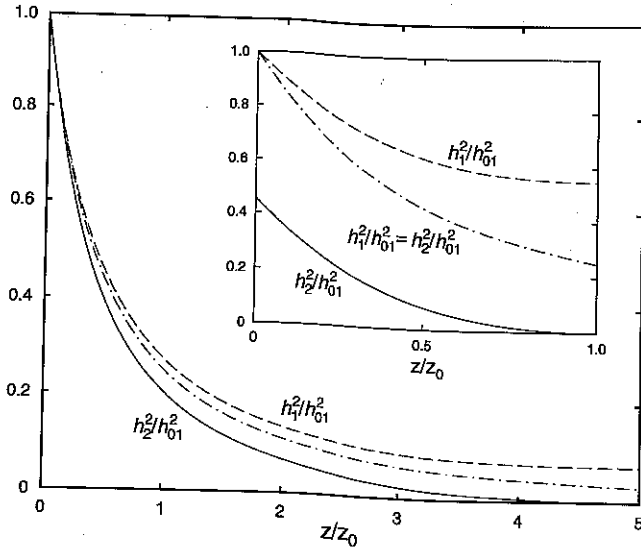
FIGURE 3 The squared amplitudes for the fundamental wave (the *dashed line*) and SHG (the *solid line*) in a lossless NIM slab of a finite length. Inset: the slab has a length equal to one conversion length. *Main plot:* the slab has a length equal to five conversion lengths. The *dash-dot lines* show the energy-conversion for a semi-infinite NIM

FIGURE 4   The difference between OPA processes in LHM and PIM slabs

Equation (21) indicates 100% conversion of the incident fundamental wave into the reflected second harmonic at $z = 0$ in a lossless semi-infinite medium provided that the phase matching condition $\Delta k = 0$ is fulfilled. The integration of (22) with the boundary condition $h_1(0) = h_{10}$ yields

$$h_2(z) = \frac{h_{10}}{(z/z_0) + 1}, \quad z_0 = (\kappa h_{10})^{-1}. \tag{23}$$

Equation (23) describes a concurrent decrease of both waves of equal amplitudes along the z-axis; this is shown by the dash-dot plots in Fig. 3. For $z \gg z_0$, the dependence is inversely proportional to z. These spatial dependencies, shown in Fig. 3, are in strict contrast with those for the conventional process of SHG in a PIM, which are known from various textbooks (compare, for example, with the lower part of Fig. 1).

3   Optical parametric amplification and difference-frequency generation in a NIM slab with absorption

3.1   *OPA: basic equations and Manley–Rowe relations*

As mentioned in Sect. 2.1, S is counterdirected with respect to k in NIMs, because $\varepsilon < 0$ and $\mu < 0$. We assume that a left-handed wave at ω_1 travels with its wavevector directed along the z-axis. Then its energy flow S_1 is directed against the z-axis. We also assume that the sample is illuminated by a higher-frequency electromagnetic wave traveling along the axis z. The frequency of this radiation ω_3 falls in a positive index range. The two coupled waves with co-directed wave-vectors k_3 and k_1 generate a difference-frequency idler at $\omega_2 = \omega_3 - \omega_1$, which has a positive refractive index. The idle wave contributes back into the wave at ω_1 through three-wave coupling and thus enables optical parametric amplification (OPA) at ω_1 by converting the energy of the pump field at ω_3. Thus, the nonlinear-optical process
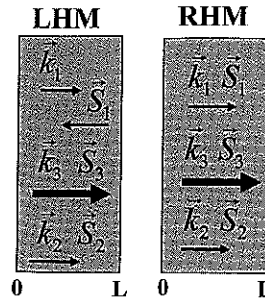
under consideration involves three-wave mixing with wave-vectors co-directed along z. Note that the energy flow of the signal wave, S_1, is directed against z, i.e., it is directed opposite to the energy flows of the two other waves, S_2 and S_3 (Fig. 4, the left part). Such a coupling scheme is in contrast with the ordinary phase-matching scheme for OPA, which is schematically shown in the right part of Fig. 4. As above, we consider the magnetic type of the quadratic nonlinearity. For the magnetic field

$$H_j(z, t) = h_j \exp[i(k_j z - \omega_j t)] + c.c., \tag{24}$$

the nonlinear magnetization at the signal and idler frequencies is given by the equations

$$M_1^{NL} = 2\chi_{eff}^{(2)} h_3 h_2^* \exp\{i[(k_3 - k_2)z - \omega_1 t]\}, \tag{25}$$

$$M_2^{NL} = 2\chi_{eff}^{(2)} h_3 h_1^* \exp\{i[(k_3 - k_1)z - \omega_2 t]\}. \tag{26}$$

Here, $j = 1, 2, 3$; $\omega_2 = \omega_3 - \omega_1$; and $k_j = |n_j|\omega_j/c > 0$. Then the equations for the slowly-varying amplitudes of the signal and the idler acquire the form

$$\frac{dh_1}{dz} = i\sigma_1 h_3 h_2^* \exp[i\Delta k z] + \frac{\alpha_1}{2} h_1, \tag{27}$$

$$\frac{dh_2}{dz} = i\sigma_2 h_3 h_1^* \exp[i\Delta k z] - \frac{\alpha_2}{2} h_2, \tag{28}$$

where $\sigma_j = 8\pi\chi_{eff}^{(2)} \varepsilon_j \omega_j^2 / k_j c^2$, $\Delta k = k_3 - k_2 - k_1$, and α_j are the absorption indices. The amplitude of the pump h_3 is assumed constant. We note the following three fundamental differences in (27) as compared with the ordinary difference-frequency generation (DFG) through the three-wave mixing of co-propagating waves in a PIM. First, the sign of σ_1 is opposite to that of σ_2 because $\varepsilon_1 < 0$. Second, the opposite sign appears with α_1 because the energy flow S_1 is directed against the z-axis. Third, the boundary conditions for h_1 are defined at the opposite side of the sample as compared to h_2 and h_3 because their energy-flows S_1 and S_2 are counter-directed.

At $\alpha_1 = \alpha_2 = 0$, one finds with the aid of (27), (28) and (5):

$$\frac{d}{dz}\left[\sqrt{\frac{\mu_1}{\varepsilon_1}}\frac{h_1^2}{\omega_1} + \sqrt{\frac{\mu_2}{\varepsilon_2}}\frac{h_2^2}{\omega_2}\right] = 0, \tag{29}$$

$$\frac{d}{dz}\left[\frac{|S_1|}{\hbar\omega_1} + \frac{|S_2|}{\hbar\omega_2}\right] = 0, \quad \frac{d}{dz}\left[\frac{S_{1z}}{\hbar\omega_1} - \frac{S_{2z}}{\hbar\omega_2}\right] = 0. \tag{30}$$

These equations represent the Manley–Rowe relations [21], which describe the creation of pairs of entangled counter-propagating photons $\hbar\omega_1$ and $\hbar\omega_2$. The equations account for the opposite sign of the corresponding derivatives with respect to z. Equation (29) predicts that the sum of the terms proportional to the squared amplitudes of signal and idler remains constant through the sample, which is in contrast with the requirement that the difference of such terms is constant in the analogous case in a PIM. We note that according to (4) and (5) the corresponding equations for the electric components in the case of the quadratic electric nonlinearity can be written in a similar form with ε_j substituted by μ_j. As seen from the equations below, this does not change either the results obtained or the main conclusions presented here; the same is true for the case of SHG. As mentioned in Sect. 2, the factors μ_j were usually assumed to be equal to unity in equations for PIMs, which is not the case for NIMs.

3.2   OPA *and* DFG *in* NIMs

We introduce the normalized amplitudes $a_j = \sqrt[4]{\varepsilon_j/\mu_j}\, h_j/\sqrt{\omega_j}$; their squared values are proportional to the number of photons at the corresponding frequencies. The corresponding equations for such amplitudes acquire the form

$$\frac{da_1}{dz} = -iga_2^* \exp[i\Delta kz] + \frac{\alpha_1}{2}a_1, \tag{31}$$

$$\frac{da_2}{dz} = iga_1^* \exp[i\Delta kz] - \frac{\alpha_2}{2}a_2, \tag{32}$$

where $g = \left(\sqrt{\omega_1\omega_2}/\sqrt[4]{\varepsilon_1\varepsilon_2/\mu_1\mu_2}\right)(8\pi/c)\chi^{(2)}h_3$. Accounting for the boundary conditions $a_1(z = L) = a_{1L}$, and $a_2(z = 0) = a_{20}$ (where L is the slab thickness), the solutions to (31) and (32) are as follows

$$a_1(z) = A_1 \exp\left[\left(\beta_1 + i\frac{\Delta k}{2}\right)z\right] + A_2 \exp\left[\left(\beta_2 + i\frac{\Delta k}{2}\right)z\right], \tag{33}$$

$$a_2^*(z) = \kappa_1 A_1 \exp\left[\left(\beta_1 - i\frac{\Delta k}{2}\right)z\right] + \kappa_2 A_2 \exp\left[\left(\beta_2 - i\frac{\Delta k}{2}\right)z\right]. \tag{34}$$

Here,

$$\beta_{1,2} = (\alpha_1 - \alpha_2)/4 \pm iR, \quad \kappa_{1,2} = [\pm R + is]/g, \tag{35}$$

$$R = \sqrt{g^2 - s^2}, \quad s = (\alpha_1 + \alpha_2)/4 - i\Delta k/2, \tag{36}$$

$$A_1 = \left\{ a_{1L}\kappa_2 - a_{20}^* \exp\left[\left(\beta_2 + i\frac{\Delta k}{2}\right)L\right]\right\}/D, \tag{37}$$

$$A_2 = -\left\{ a_{1L}\kappa_1 - a_{20}^* \exp\left[\left(\beta_1 + i\frac{\Delta k}{2}\right)L\right]\right\}/D, \tag{38}$$

$$D = \kappa_2 \exp\left[\left(\beta_1 + i\frac{\Delta k}{2}\right)L\right] - \kappa_1 \exp\left[\left(\beta_2 + i\frac{\Delta k}{2}\right)L\right]. \tag{39}$$

At $a_{20} = 0$, the amplification factor for the left-handed wave is given by $\eta_a(\omega_1) = |a_{10}/a_{1L}|^2$, where

$$\frac{a_{10}}{a_{1L}} = \frac{\exp\left[-\left(\dfrac{\alpha_1 - \alpha_2}{4} + i\dfrac{\Delta k}{2}\right)L\right]}{\cos RL + \left[\dfrac{\alpha_1 + \alpha_2}{4R} - i\dfrac{\Delta k}{2R}\right]\sin RL}. \tag{40}$$

Alternatively, at $a_{1L}^* = 0$, the conversion factor for the difference-frequency generation of the left-handed wave is found as $\eta_g(\omega_1) = |a_{10}/a_{20}^*|^2$, where

$$\frac{a_{10}}{a_{20}^*} = \frac{-(g/R)\sin RL}{\cos RL + \left[\dfrac{\alpha_1 + \alpha_2}{4R} - i\dfrac{\Delta k}{2R}\right]\sin RL}. \tag{41}$$

Equation (40) shows that the amplification of the left-handed wave can be turned into a cavity-less oscillation when the denominator tends to zero. The conversion factor for DFG, η_g, experiences a similar increase. In the case of $\Delta k = 0$ and small optical losses $(\alpha_1 + \alpha_2)L \ll \pi$, (33) and (34) are reduced to

$$a_1^*(z) \approx \frac{a_{1L}^*}{\cos(gL)}\cos(gz) + \frac{ia_{20}}{\cos(gL)}\sin[g(z - L)], \tag{42}$$

$$a_2(z) \approx \frac{ia_{1L}^*}{\cos(gL)}\sin(gz) + \frac{a_{20}}{\cos(gL)}\cos[g(z - L)]. \tag{43}$$

The output amplitudes are then given by

$$a_{10}^* = \frac{a_{1L}^*}{\cos(gL)} - ia_{20}\tan(gL), \tag{44}$$

$$a_{2L} = ia_{1L}^*\tan(gL) + \frac{a_{20}}{\cos(gL)}. \tag{45}$$

Thus, the oscillation threshold value for the control field intensity in this case is given by $g_t = \pi/2L$. It increases with absorption and phase mismatch.

The dependence of the output intensity for the left-handed wave propagating in an absorptive NIM slab in the presence of the control field at ω_3 and at $a_{20} = 0$ is shown by the solid line in Fig. 5 for two representative cases of exact and partial phase-matching. The dash plots show the output in the case of DFG (at $a_{1L} = 0$, $a_{2,0} \neq 0$). Amplification in the upper part of Fig. 5 reaches many orders in the first maximum and increases in the next maximums. It can be seen that the amplification can entirely compensate for absorption and even turn into oscillations when the intensity of the control field reaches values given by a periodic set of increasing numbers. The larger the corresponding value, the greater the amplification and the DFG output; the latter depends on the absorption for both waves and on the phase mismatch Δk. The conversion factor is larger in its maximums than the amplification factor because DFG is a one-step process, whereas OPA is a two-step process as discussed in Sect. 3.1. As seen from Fig. 5, the output shows a resonance dependence on the intensity of the control field at ω_3. Figure 6 depicts corresponding changes in the distribution of the negative-index field inside the slab in the vicinity of the first maximum at $\Delta k = 0$.
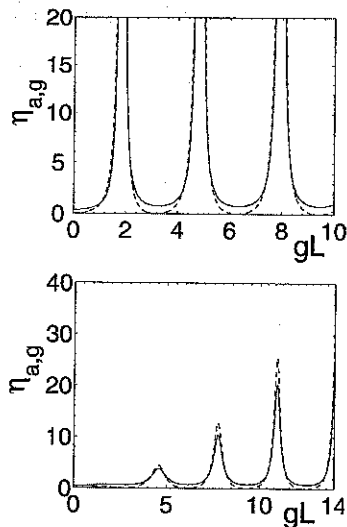
FIGURE 5 The amplification factor $\eta_a(\omega_1)$ (the *solid line*) and the efficiency of difference-frequency generation $\eta_g(\omega_1)$ (the *dashed line*) for the backward wave at $z = 0$. $\alpha_1 L = 1$, $\alpha_2 L = 1/2$. In the *upper plot*: $\Delta k = 0$. In the *lower plot* $\Delta k = \pi$
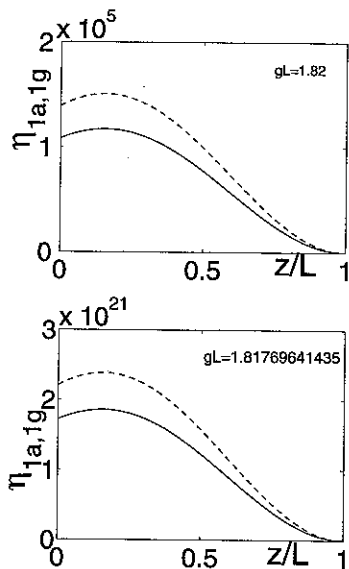

FIGURE 6 Resonant changes in the distribution of the normalized intensity of the left-handed wave inside the slab of NIM, $\eta_a(\omega_1)$ (the *solid line*) and $\eta_g(\omega_1)$ (the *dashed line*), caused by the adjustment of the normalized intensity for the control field at ω_3, gL. $\alpha_1 L = 1$, $\alpha_2 L = 1/2$, $\Delta k = 0$

4　　Conclusion

We have studied the unusual properties of second-harmonic generation (SHG) in metamaterials that have a negative refractive index for the fundamental wave and a positive index for its second harmonic (SH). The possibility of a left-handed nonlinear-optical mirror, which converts the incoming radiation into a reflected beam at the doubled frequency with efficiency that can approach 100% for lossless and phase-matched medium is considered. The most striking differences in the nonlinear propagation and the spatial dependence of the energy-conversion process for SHG in NIMs, as compared to PIMs, can be summarized as follows. In NIMs, the intensities of the fundamental and SH waves both decrease

along the medium. Such unusual dependence and the apparent contradiction with the ordinary Manley–Rowe relations are explained by the fact that the energy flows for the fundamental and SH waves are counter-directed, whereas their wave-vectors are co-directed. Another interesting characteristic of SHG in NIMs is that the energy conversion at any point within a NIM slab depends on the total thickness of the slab. This is because SHG in a NIM is determined by the boundary condition for SH at the rear interface rather than the front interface of the slab.

We have shown the feasibility of compensating losses in NIMs by optical parametric amplification (OPA). In this process, the wave-vectors of all three coupled waves are co-directed, whereas the energy flow for the signal wave is counter-directed with respect to those for the pump and the idler waves. This process is characterized by properties that are in strict contrast with those known for conventional nonlinear-optical crystals. Such extraordinary features allow one to realize optical parametric oscillations (OPOs) without a cavity at frequencies where the refractive index is negative. We also showed that the OPA and OPO in NIMs enable the generation of pairs of entangled counter-propagating right- and left-handed photons inside the NIM slabs.

The backward energy flow for one of the coupled waves (whereas the wave-vectors of all the coupled waves are co-directed) is inherent for NIMs and it makes this process different from three-wave mixing in PIMs. This is also different from various processes in RHMs based on distributed gratings and feedback. The important advantage of the backward OPA and OPO in NIMs investigated here is the distributed feedback, which enables oscillations without a cavity. In NIMs, each spatial point serves as a source for the generated wave in the reflected direction, whereas the phase velocities of all the three coupled waves are co-directed. As mentioned, it is very hard to realize such a scheme in PIMs, while the OPA in NIMs proposed herein is free from the PIM limitations.

REFERENCES

1 V.M. Shalaev, W. Cai, U. Chettiar, H.-K. Yuan, A.K. Sarychev, V.P. Drachev, A.V. Kildishev, Opt. Lett. **30**, 3356 (2005), first reported in arXiv: physics/0504091 (April 13, 2005)
2 S. Zhang, W. Fan, N.C. Panoiu, K.J. Malloy, R.M. Osgood, S.R.J. Brueck, Phys. Rev. Lett. **95**, 137404 (2005), arXiv: physics/0504208 (2005)
3 A. Berrier, M. Mulot, M. Swillo, M. Qiu, L. Thylén, A. Talneau, S. Anand, Phys. Rev. Lett. **93**, 73902 (2004)
4 E. Schonbrun, M. Tinker, W. Park, J.-B. Lee, IEEE Photon. Technol. Lett. **17**, 1196 (2005)
5 V.G. Veselago, Sov. Phys. Solid State **8**, 2854 (1967)
6 V.G. Veselago, Usp. Fiz. Nauk **92**, 517 (1967) [Sov. Phys. Usp. **10**, 509 (1968)]
7 S. Linden, C. Enkrich, M. Wegener, J. Zhou, T. Koschny, C.M. Soukoulis, Science **306**, 1351 (2004)
8 Z. Zhang, W. Fan, B.K. Minhas, A. Frauenglass, K.J. Malloy, S.R.J. Brueck, Phys. Rev. Lett. **94**, 037402 (2005)

9   A.N. Grigorenko, A.K. Geim, N.F. Gleeson, Y. Zhang, A.A. Firsov, I.Y. Khrushchev, J. Petrovic, Nature **438**, 335 (2005)

10   M. Lapine, M. Gorkunov, K.H. Ringhofer, Phys. Rev. E **67**, 065601 (2003)

11   A.A. Zharov, I.V. Shadrivov, Y.S. Kivshar, Phys. Rev. Lett. **91**, 037401 (2003)

12   M. Lapine, M. Gorkunov, Phys. Rev. E **70**, 66601 (2004)

13   N.A. Zharova, I.V. Shadrivov, A.A. Zharov, Y.S. Kivshar, Opt. Express **13**, 1291 (2005)

14   V.M. Agranovich, Y.R. Shen, R.H. Baughman, A.A. Zakhidov, Phys. Rev. B **69**, 165112 (2004)

15   A.A. Zharov, N.A. Zharova, Il.V. Shadrivov, Y.S. Kivshar, Appl. Phys. Lett. **87**, 091104 (2005)

16   A.B. Kozyrev, H. Kim, A. Karbassi, D.W. van der Weide, Appl. Phys. Lett. **87**, 121109 (2005)

17   I.V. Shadrivov, A.A. Zharov, Y.S. Kivshar, arXiv: physics/0506092 (2005)

18   S.E. Harris, Appl. Phys. Lett. **9**, 114 (1966)

19   K.I. Volyak, A.S. Gorshkov, Radiotekhnika Elektronika (Radiotechnics Electronics) **18**, 2075 (1973) (Moscow, in Russian)

20   A. Yariv, *Quantum Electronics*, 2nd edn. (Wiley, New York, 1975)

21   J.M. Manley, H.E. Rowe, Proc. IRE **47**, 2115 (1959)